

electronic structure and tunneling probability of the different CO molecules. We illustrate this by calculating the tunneling current probability using the standard Bardeen approximation [equations 2 and 3 in (23)] and the calculated partial density of states (DOS) for CO molecules on the cluster and on the tip (fig. S6) (23). The calculation reveals that the CO molecules on the corners indeed have greater tunneling contributions than the CO molecules on the edges, qualitatively explaining the experimentally observed contrast of the STM images with the six bright spots plus one in the center, as shown in Fig. 2, B and D. We could explain the threefold symmetry of some of the 19 atom clusters by adding three Cu atoms at the center of the 19 atoms. These three low-coordinated Cu atoms, producing the bright center of the cluster images, can bind three additional CO molecules and distort the tilt angles of the peripheral CO molecules, as shown in Fig. 2, C and E [(details are shown in (23))].

Finally, we investigated the effect of clustering on surface reactivity for the WGS reaction (i.e., $\text{CO} + \text{H}_2\text{O} \leftrightarrow \text{CO}_2 + \text{H}_2$), which Cu catalyzes. Water does not adsorb on the Cu(111) surface at room temperature (Fig. 4B) (32), whereas it dissociatively adsorbs on the more active Cu(110) surface (32). Once the gas phase CO at 1 Torr was pumped away, the STM images revealed that the Cu clusters were still present, although atomic resolution could not be achieved, likely because of the absence of CO molecules adsorbed on the tip in high vacuum (Fig. 3A). In the presence of 2×10^{-9} Torr of H_2O , the cluster-covered surface was very active in dissociating water, as shown by the increasing oxygen peak in both the Auger electron spectra (AES) shown in Fig. 3B, and in the XPS spectra shown in Fig. 3C. The APXPS spectrum indicates that the O peak is a result of the dissociative adsorption of H_2O (Fig. 4A) and that no such peak appears after experiments at 0.1 Torr of CO because clustering of the Cu did not occur at lower CO pressures (Figs. 1B and 3B). A similar effect was also observed during exposure to $\text{CO} + \text{H}_2\text{O}$ mixtures, as shown in Fig. 4A. The pristine Cu(111) surface, on the other hand, not pre-exposed to CO, is inactive (Fig. 4B).

Our findings open the possibility that other soft materials (e.g., Ag, Au, and Zn) can similarly undergo large reconstructions at sufficiently high pressures of CO (or other molecules). We have also demonstrated that the inactive (111) face of Cu for water dissociation, a key step in the water-gas shift reaction, becomes highly activated as a result of the CO-induced clustering. The need for this type of study to extend our understanding of the working of catalysts under operating conditions is clear.

REFERENCES AND NOTES

- G. A. Somorjai, *Introduction to Surface Chemistry and Catalysis* (Wiley-VCH, 1999).
- G. Ertl, *Angew. Chem. Int. Ed.* **47**, 3524–3535 (2008).
- B. J. McIntyre, M. Salmeron, G. A. Somorjai, *Rev. Sci. Instrum.* **64**, 687–691 (1993).
- L. Österlund et al., *Phys. Rev. Lett.* **86**, 460–463 (2001).
- E. Laegsgaard et al., *Rev. Sci. Instrum.* **72**, 3537–3542 (2001).
- F. Tao, D. Tang, M. Salmeron, G. A. Somorjai, *Rev. Sci. Instrum.* **79**, 084101 (2008).
- F. Besenbacher, P. Thstrup, M. Salmeron, *MRS Bull.* **37**, 677–681 (2012).
- C. T. Herbschleb et al., *Rev. Sci. Instrum.* **85**, 083703 (2014).
- M. Salmeron, R. Schlögl, *Surf. Sci. Rep.* **63**, 169–199 (2008).
- M. Salmeron, *MRS Bull.* **38**, 650–657 (2013).
- K. Klier, in *Advances in Catalysis*, Vol. 31, D. D. Eley, H. Pines, P. B. Weisz, Eds. (Academic Press, 1982), pp. 243–313.
- D. S. Newsome, *Catal. Rev.* **21**, 275–318 (1980).
- J. Szanyi, D. W. Goodman, *Catal. Lett.* **10**, 383–390 (1991).
- J. Yoshihara, C. T. Campbell, *J. Catal.* **161**, 776–782 (1996).
- M. Behrens et al., *Science* **336**, 893–897 (2012).
- G. A. Olah, *Angew. Chem. Int. Ed.* **52**, 104–107 (2013).
- M. Behrens, *Angew. Chem. Int. Ed.* **53**, 12022–12024 (2014).
- K. Kambe, *Phys. Rev.* **99**, 419–422 (1955).
- C. Kittel, *Introduction to Solid State Physics*, 8th Edition (Wiley, 2005).
- S. R. Longwitz et al., *J. Phys. Chem. B* **108**, 14497–14502 (2004).
- D. Tang, K. S. Hwang, M. Salmeron, G. A. Somorjai, *J. Phys. Chem. B* **108**, 13300–13306 (2004).
- F. Tao et al., *Science* **327**, 850–853 (2010).
- See supplementary materials on Science Online.
- B. Eren et al., *J. Phys. Chem. C* **119**, 14669–14674 (2015).
- J. Lagoutte, X. Liu, S. Fölsch, *Phys. Rev. Lett.* **95**, 136801 (2005).
- O. V. Lyssenko, V. S. Stepanyuk, W. Hergert, J. Kirschner, *Phys. Rev. Lett.* **89**, 126102 (2002).
- M. Mehlhorn, H. Gawronski, K. Morgenstern, *Phys. Rev. Lett.* **104**, 076101 (2010).
- H. J. Yang, T. Minato, M. Kawai, Y. Kim, *J. Phys. Chem. C* **117**, 16429–16437 (2013).
- L. Bartels, D. Meyer, K. H. Rieder, *Surf. Sci. Lett.* **432**, L621–L626 (1999).
- M. Poensgen, J. F. Wolf, J. Frohn, M. Giesen, H. Ibach, *Surf. Sci.* **274**, 430–440 (1992).
- M. M. Waldrop, *Science* **234**, 673–674 (1986).
- S. Yamamoto et al., *J. Phys. Chem. C* **111**, 7848–7850 (2007).

ACKNOWLEDGMENTS

This work was supported by the Office of Basic Energy Sciences (BES), Division of Materials Sciences and Engineering, of the U.S. Department of Energy (DOE) under contract no. DE-AC02-05CH11231, through the Chemical and Mechanical Properties of Surfaces, Interfaces and Nanostructures program (FWP KC3101). It used resources of the National Energy Research Scientific Computing Center and the Advanced Light Source, which are supported by the Office of Science of the U.S. DOE. The computation used resources from the Oak Ridge Leadership Computing Facility (OLCF), with time allocated by the Innovative and Novel Computational Impact on Theory and Experiment (INCITE) project.

SUPPLEMENTARY MATERIALS

www.sciencemag.org/content/351/6272/475/suppl/DC1
Materials and Methods
Supplementary Text
Figs. S1 to S8
Tables S1 to S3
References (33–41)

16 November 2015; accepted 14 December 2015
10.1126/science.aad8868

OCEANOGRAPHY

Enhanced East Pacific Rise hydrothermal activity during the last two glacial terminations

D. C. Lund,^{1*} P. D. Asimow,² K. A. Farley,² T. O. Rooney,³ E. Seeley,¹ E. W. Jackson,⁴ Z. M. Durham⁴

Mid-ocean ridge magmatism is driven by seafloor spreading and decompression melting of the upper mantle. Melt production is apparently modulated by glacial-interglacial changes in sea level, raising the possibility that magmatic flux acts as a negative feedback on ice-sheet size. The timing of melt variability is poorly constrained, however, precluding a clear link between ridge magmatism and Pleistocene climate transitions. Here we present well-dated sedimentary records from the East Pacific Rise that show evidence of enhanced hydrothermal activity during the last two glacial terminations. We suggest that glacial maxima and lowering of sea level caused anomalous melting in the upper mantle and that the subsequent magmatic anomalies promoted deglaciation through the release of mantle heat and carbon at mid-ocean ridges.

Sea level–driven pressure variations due to the growth and decay of ice sheets likely modulate melt production in the upper mantle on Milankovitch time scales (1, 2). Model simulations suggest that the magnitude of the resulting signal at mid-ocean ridges depends on the plate spreading rate, the melt extraction velocity, and the thermal properties of the lithosphere (1, 3). Because of the slow rate of melt migration in the upper mantle, the magmatic signal at ridges probably lags changes in sea level by thousands of years (1). Surveys of

ridge bathymetry reveal Milankovitch-scale frequencies in abyssal-hill spacing, consistent with the sea-level hypothesis (3, 4). Bathymetry records are subject to geological damping effects and

¹Department of Marine Sciences, University of Connecticut, Groton, CT 06340, USA. ²Division of Geological and Planetary Sciences, California Institute of Technology, Pasadena, CA 91125, USA. ³Department of Geological Sciences, Michigan State University, East Lansing, MI 48824, USA. ⁴Department of Earth and Environmental Sciences, University of Michigan, Ann Arbor, MI 48109, USA.

*Corresponding author. E-mail: david.lund@uconn.edu

substantial age uncertainties, however, and they therefore require validation with other proxies. Because hydrothermal activity along ridge sections is ultimately driven by magmatic heat, sedimentary records of hydrothermal output can be used to assess the sea-level hypothesis and determine the timing of magmatic anomalies relative to key Pleistocene climate transitions.

The southern East Pacific Rise (SEPR) has the fastest spreading rate and the highest magmatic budget of any ridge in the global mid-ocean ridge system (5). Due to its elevated magmatism, the SEPR has over 50 known active vent sites from 5°S to 37°S (6), consistent with the global trend in plume incidence versus magmatic budget for ridges spanning a range of spreading rates (5, 7). Intense hydrothermal venting and topographically steered flow of plumes along the SEPR create a spatially integrated pattern of metalliferous sediments near the ridge crest (8–10). Compared with slower ridges, SEPR sediments have anomalously high metal concentrations (8, 11), suggesting that magmatism is the primary factor governing hydrothermal input to these sedimentary archives on geologic time scales. Hydrothermal plume par-

ticles are highly enriched in elements that are derived directly from vents and scavenged from seawater. Variations in the flux of these elements to ridge-flank sediments should therefore reflect long-term changes in hydrothermal activity.

We used a multiproxy geochemical strategy to reconstruct SEPR hydrothermal activity during the last glacial cycle. We analyzed a total of seven ridge-crest cores from 6°S and 11°S, where the half-spreading rate averages 75 mm/year (Fig. 1). Together with two published records from near the East Pacific Rise (EPR)–Dietz volcanic-ridge triple junction at 1°N (12), the locations span a range of spreading rates, sedimentary environments, and surface-ocean productivity regimes. To control for spatial heterogeneity in plume incidence versus magmatic budget (7), the sampling locations span three separate EPR segments. At each segment, we analyzed cores from both sides of the ridge axis to address potential biases due to horizontal sediment focusing, bioturbation, and spatial variability in hydrothermal-plume direction. Radiocarbon and oxygen isotopic analyses of planktonic foraminifera provided age control for each core (13). Major and trace ele-

ment concentrations were determined using x-ray fluorescence (XRF) and inductively coupled plasma mass spectrometry (ICP-MS). The fluxes of hydrothermal components were estimated using both mass accumulation rates and the ^3He normalization method (13). Given that plume particles primarily consist of Fe oxyhydroxides and Mn oxides (14), we used sedimentary Fe and Mn to track hydrothermal inputs. To cross-check the Fe and Mn results, we also measured arsenic, which is scavenged from seawater by Fe oxyhydroxides and varies coherently with Fe in hydrothermal-plume particles (15) and SEPR sediments (16).

Oxygen stable isotope records from 1°N, 6°S, and 11°S outline marine isotope stages 1, 2, and 3, indicating that there has been minimal stratigraphic disturbance of the cores due to sediment winnowing or downslope transport (Fig. 2). The flux of Fe in all nine records peaks between 10 and 20 thousand years before the present (ky B.P.). Manganese fluxes to EPR sediments follow a similar pattern, with maximum values centered at ~15 ky B.P. Arsenic fluxes at 6°S and 11°S reach a maximum between 10 and 20 ky B.P., supporting the Fe and Mn results. Offsets between time series are generally 5 ky or less (Fig. 2), similar to the age uncertainty associated with the mass accumulation rate method (13). Results from the ^3He normalization technique, which yields fluxes that are insensitive to age-model uncertainty, show that positive shifts in metal fluxes at 11°S and 6°S occurred within 2 ky of one another (fig. S1). Thus, the overall pattern for the past 50 ky is one of coherent variations in hydrothermal sedimentation along 1300 km of the EPR, with maximum metal inputs coinciding with the last deglaciation (Termination I).

Two cores at 11°S span the penultimate deglaciation (Termination II), including core Y71-07-53 on the western flank of the SEPR and core Y71-07-47 on the eastern flank (Fig. 3). Metal fluxes are higher in the western-flank core, consistent with the east-west contrast in the shorter records (Fig. 2) and the spatial pattern in metal concentrations of late Holocene sediments (8). In the western-flank core, the flux of each metal increases markedly at ~140 ky B.P., reaches a maximum by 130 ky B.P., and then returns to background levels by 120 ky B.P. (Fig. 3). A similar pattern occurs in the eastern-flank core. The contemporaneous signal at these locations indicates that hydrothermal inputs on each side of the ridge crest varied in phase. The records also show that the maximum flux of hydrothermal metals coincided with Termination II, similar to the pattern for Termination I.

Diagenetic overprinting, horizontal sediment focusing, and dilution with nonhydrothermal components can complicate the interpretation of hydrothermal proxies. Diagenetic remobilization should influence Fe oxyhydroxides and MnO_2 differently, given the large offset in their redox potentials (17), yet we observed coherent down-core variations in Fe, Mn, and As, regardless of location. Furthermore, down-core Fe/Mn ratios generally fall within the expected range for hydrothermal input (8). Anomalously high

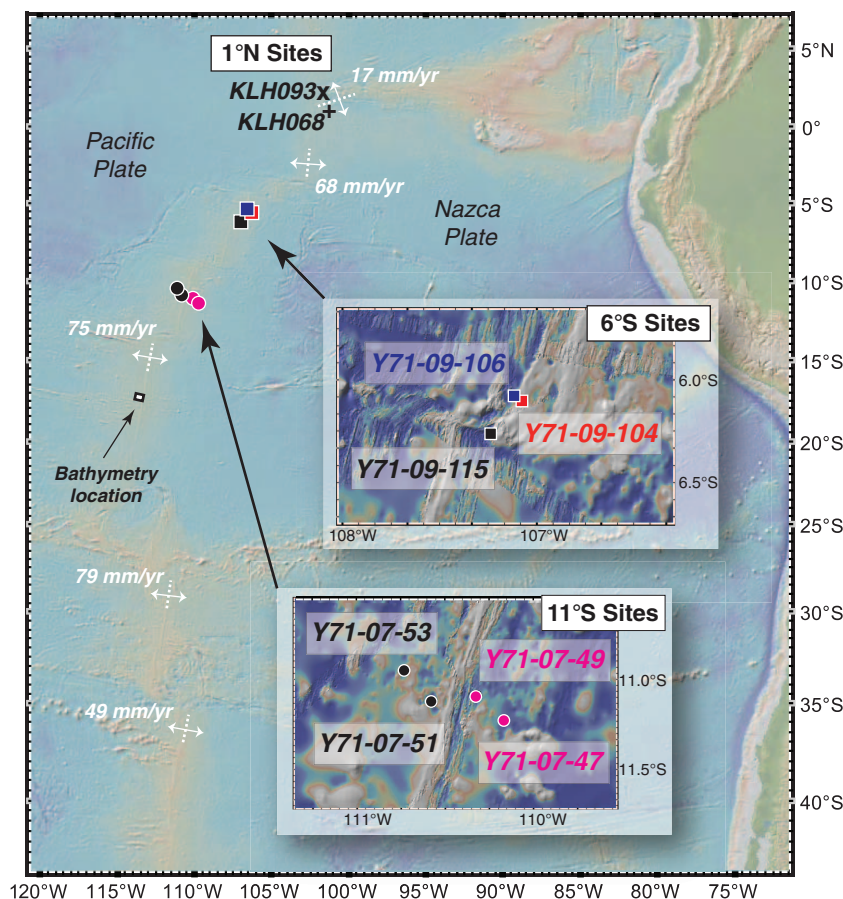


Fig. 1. Map of sampling sites near the EPR. Core locations include 1°N (cores KLH068 and KLH093) (12), 6°S (core Y71-09-104 in blue, Y71-09-106 in red, and Y71-09-115 in black), and 11°S (cores Y71-07-47 and Y71-07-49 in magenta and Y71-07-51 and Y71-07-53 in black). Also shown is the location of the bathymetry record at 17°S (4). Half-spreading rates are shown in white (www.ideo.columbia.edu/~menke/plates.html). The half-spreading rate at 1°N (17 mm/year measured at Dietz volcanic ridge) is from (29). The map was generated using GeoMapApp (www.geomapapp.org).

Fe/Mn ratios at 1°N are probably due to suboxic diagenesis and Mn remobilization (13). At the 1°N locations, near-zero Mn levels before 20 kyr BP are likely driven by MnO₂ reduction and upward migration of dissolved Mn²⁺. Nevertheless, the overall coherent pattern in Fe records from the high-productivity equatorial Pacific (1°N) to the northern edge of the subtropical gyre (11°S) indicates that the organic carbon flux to the sediments is not a first-order control on down-core metal variability. Sediment focusing is an equally unlikely explanation, given the similar pattern in multiple cores from a range of sedimentary environments. Focusing factors estimated using ³He also show no evidence for anomalous horizontal sediment transport during Termination I (fig. S3). Lastly, the ³He-based metal

fluxes are consistent with the mass accumulation rate results, indicating that carbonate dilution was not a primary driver of the down-core signal. Taken together, these lines of evidence indicate that the metal fluxes primarily reflect the input of hydrothermal plume particles to ridge-crest sediments.

The temporal variability in metal fluxes is similar to that in seafloor bathymetry at 17°S on the SEPR, implying that both have a common driver (Fig. 4). A lowering of sea level due to ice-sheet expansion would promote decompression melting in the upper mantle. The resulting increase in melt delivery to the ridge crest should result in shoaling of the bathymetry and greater hydrothermal activity (1, 3). Ice-sheet retreat and rising sea level would have the opposite effect. Shallower bathymetry on the SEPR generally

corresponds to elevated hydrothermal fluxes, consistent with the expected pattern (Fig. 4). The bathymetry record lags the hydrothermal proxies by ~10 kyr, however (fig. S4). The offset is most likely due to age uncertainty in the bathymetry time series, where the age model is based on a half-spreading rate that optimizes the match between the bathymetry and atmospheric CO₂ records (4). More generally, age constraints for late Pleistocene oceanic crust are limited to two control points, an assumed zero age at the ridge crest and the Brunhes-Matuyama boundary at 780 kyr B.P. Even if reliable absolute ages were available for individual abyssal hills, it is unlikely that their bathymetry would reflect only the melt delivery that occurred when that oceanic crust was at the ridge crest, because of the confounding influences of lower crustal accretion, surface

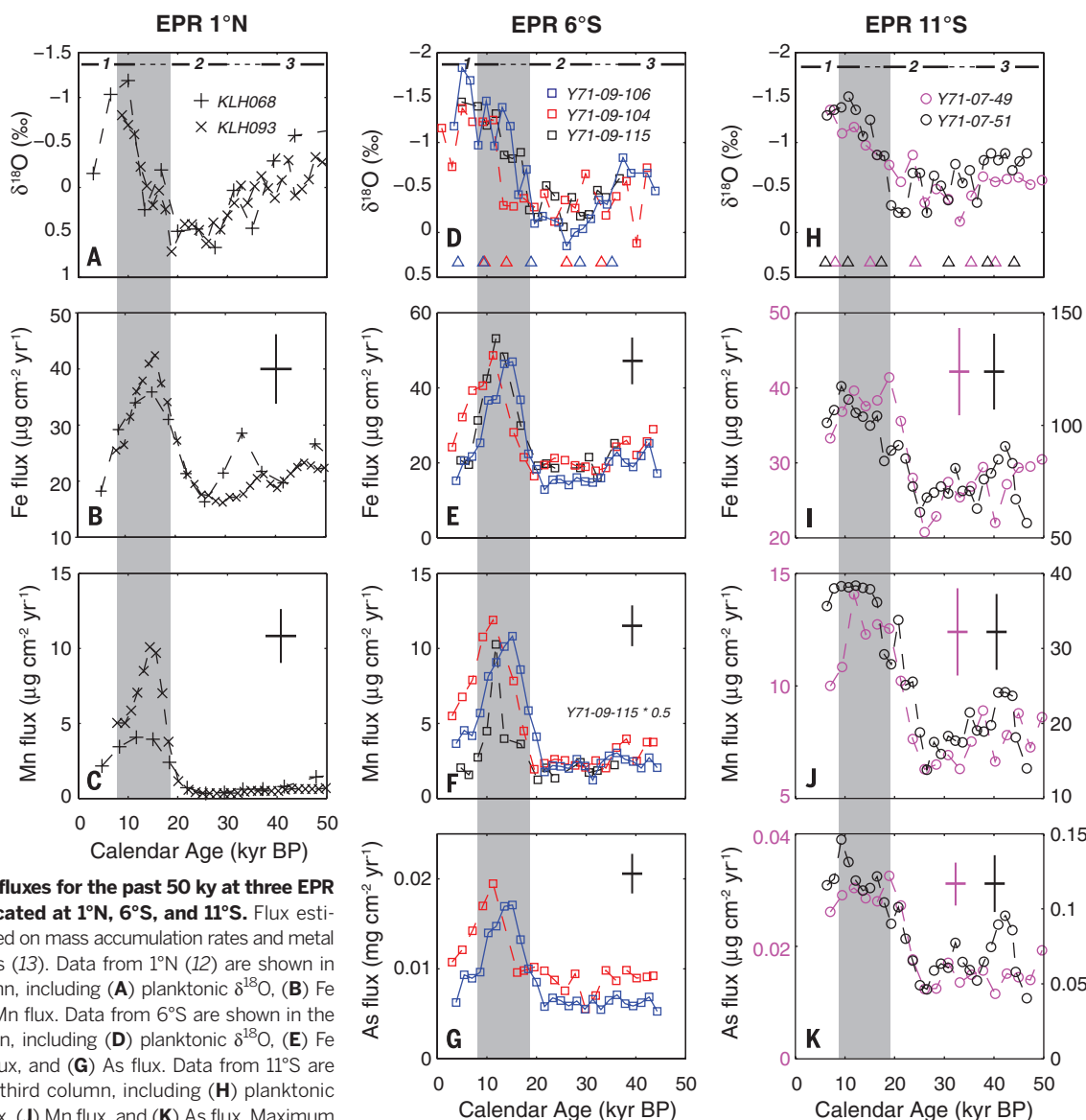


Fig. 2. Metal fluxes for the past 50 kyr at three EPR segments located at 1°N, 6°S, and 11°S. Flux estimates are based on mass accumulation rates and metal concentrations (13). Data from 1°N (12) are shown in the first column, including (A) planktonic $\delta^{18}\text{O}$, (B) Fe flux, and (C) Mn flux. Data from 6°S are shown in the second column, including (D) planktonic $\delta^{18}\text{O}$, (E) Fe flux, (F) Mn flux, and (G) As flux. Data from 11°S are shown in the third column, including (H) planktonic $\delta^{18}\text{O}$, (I) Fe flux, (J) Mn flux, and (K) As flux. Maximum fluxes occur during Termination I (gray vertical bar). Typical errors for each record (crosses in each panel) represent the uncertainty of the flux estimates (vertical line) and age model error (horizontal line). Calendar-corrected radiocarbon ages are shown as triangles. Approximate time intervals for marine isotope stages 1 to 3 are indicated in the top row of panels. Arsenic results are not available for cores collected at 1°N because these cores were analyzed using XRF rather than ICP-MS (12).

lava flows, and vertical and horizontal offsets of crustal blocks by faulting (3, 4, 18, 19). Although bathymetric time series are useful for identifying Milankovitch frequencies, the absolute timing of events is poorly constrained by these records. Hydrothermal proxies, on the other hand, can be accurately dated using radiocarbon and oxygen isotope stratigraphy. As a result, we are able to infer that intervals of intense hydrothermal activity on the EPR occurred during the last two glacial terminations.

The coincidence in timing between hydrothermal maxima and glacial terminations implies that there may be a direct causal relationship between sea-level rise and hydrothermal activity. Our understanding of the physical mechanisms of decompression melting and melt migration to the ridge axis suggests a more complex relationship, however. Proxies of magmatic flux should

lag sea-level changes by thousands of years, because of the slow rate of melt migration from the magma source region to the ridge axis (1). During the Last Glacial Maximum, the maximum rate of sea-level decrease (and hence of pressure release in the melting regime) occurred between 30 and 25 ky B.P. (20), or 15 ± 5 ky before the inferred maximum in EPR hydrothermal activity (Fig. 2). We observed a similar lag between the maximum rate of sea-level rise at ~ 15 ky B.P. (20) and the late Holocene minimum in metal flux. Assuming an average melt origin depth of 50 km (21), the implied melt extraction velocities range from 2.5 to 5 m/year, which is consistent with the rate of >1 m/year implied by U/Th disequilibrium in zero-age mid-ocean ridge basalts (22) but much lower than the estimates of >50 m/year based on the time lag between deglaciation and volcanism in Iceland (23). Our estimate is inde-

pendent of previous methods and provides a range of constraints for refining models of melt extraction at fast spreading centers.

Our results support the hypothesis that enhanced ridge magmatism, hydrothermal output, and perhaps mantle CO_2 flux act as a negative feedback on ice-sheet size (1, 4). Although the modern carbon output from ridges is small (0.02 to 0.2 Pg C/year) (24), the flux probably increased as a result of sea-level modulation. Carbon sources at off-axis locations, backarc basins, and island arcs may also amplify the mid-ocean ridge signal (2). The long melt-migration times for carbon-rich melts may lead to considerable differences in timing between hydrothermal and carbon-flux variations, however (25). Another mechanism whereby magmatic variations may influence climate is the hydrothermal heat flux itself. Enhanced geothermal heat flux should warm and destabilize the deep ocean (26), with excess heat emerging along isopycnals into the surface Southern Ocean (26, 27). Temperatures in the deep

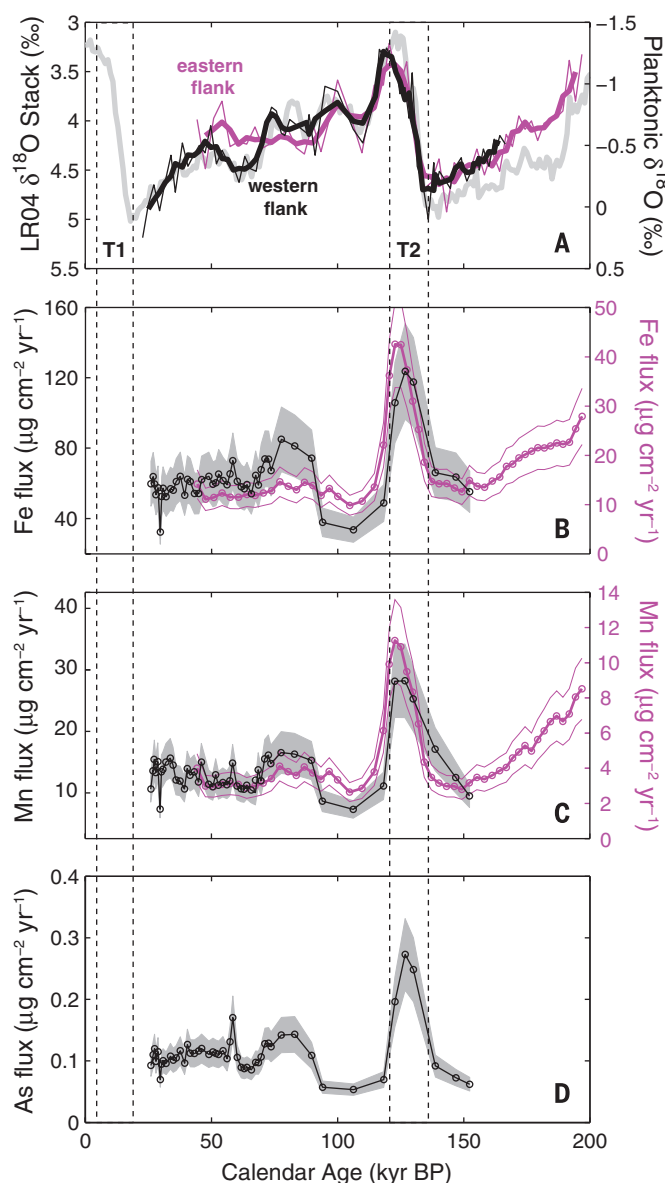


Fig. 3. Planktonic $\delta^{18}\text{O}$ and metal fluxes spanning Termination II at 11°S .

The time series are from the eastern (core Y71-07-47; magenta) and western (core Y71-07-53; black) flanks of the EPR. (A) Planktonic $\delta^{18}\text{O}$ results superimposed on a global benthic $\delta^{18}\text{O}$ stack [LR04 (30)] (gray line). (B) Fe flux, (C) Mn flux, and (D) As flux. In (A), thin lines indicate data from discrete samples, and thick lines indicate time series smoothed with a three-point running mean. In (B) to (D), flux estimates are based on mass accumulation rates and metal concentrations. Glacial terminations are indicated by dashed vertical lines. Hydrothermal metal fluxes peaked during Termination II (T2). Error bars for the western flank (gray shaded area) and eastern flank (thin magenta lines) reflect the uncertainty of the flux estimates in (B) to (D) (13). Metal data for core Y71-07-53 (16) were assigned ages based on the $\delta^{18}\text{O}$ stratigraphy generated for this work. Arsenic data are not available for core Y71-07-47 because it was analyzed using XRF rather than ICP-MS.

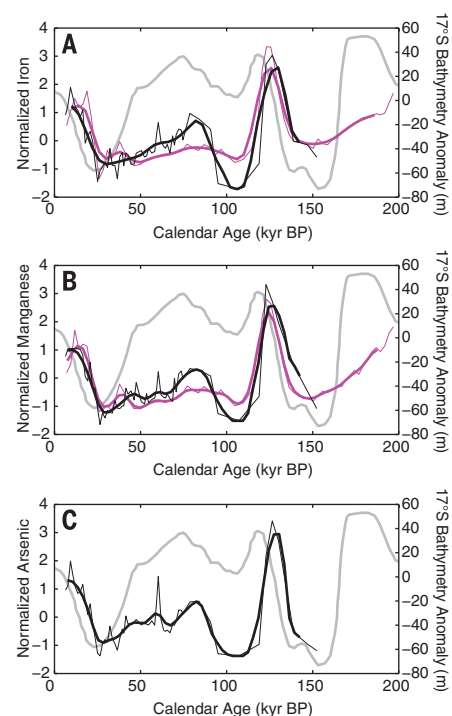


Fig. 4. Normalized metal fluxes at 11°S compared with EPR bathymetry. The hydrothermal time series are from the eastern (magenta) and western (black) flanks of the EPR and include (A) Fe flux, (B) Mn flux, and (C) As flux. We normalized each record by subtracting the mean and dividing by the standard deviation of each time series to facilitate comparison between cores with different mean metal concentrations. The results include both discrete samples (thin lines) and time series smoothed with a 20-ky-wide Gaussian window (thick lines) to approximate the resolution of the bathymetry compilation at 17°S (gray lines) (4). Fluxes from 0 to 40 ky are based on the results from Fig. 2; the interval from 40 to 200 ky B.P. is based on results shown in Fig. 3.

eastern tropical Pacific and Antarctica peaked during each of the last two glacial terminations (28), consistent with the timing of enhanced EPR hydrothermal activity.

Isolating a mechanistic linkage between ridge magmatism and glacial terminations will require a suite of detailed proxy records from multiple ridges that are sensitive to mantle carbon and geothermal inputs, as well as modeling studies of their influence in the ocean interior. The EPR results establish the timing of hydrothermal anomalies, an essential prerequisite for determining whether ridge magmatism can act as a negative feedback on ice-sheet size. The data presented here demonstrate that EPR hydrothermal output increased after the two largest glacial maxima of the past 200,000 years, implicating mid-ocean ridge magmatism in glacial terminations.

REFERENCES AND NOTES

- D. C. Lund, P. D. Asimow, *Geochem. Geophys. Geosyst.* **12**, Q12009 (2011).
- P. Huybers, C. Langmuir, *Earth Planet. Sci. Lett.* **286**, 479–491 (2009).
- J. W. Crowley, R. F. Katz, P. Huybers, C. H. Langmuir, S. H. Park, *Science* **347**, 1237–1240 (2015).
- M. Tolstoy, *Geophys. Res. Lett.* **42**, 1346–1351 (2015).
- E. T. Baker, G. R. German, in *Mid-Ocean Ridges: Hydrothermal Interactions Between the Lithosphere and Oceans*, C. R. German, J. Lin, L. M. Parson, Eds. (Geophysical Monograph Series vol. 148, American Geophysical Union, 2004), pp. 245–266.
- S. E. Beaulieu, E. T. Baker, C. R. German, A. Maffei, *Geochem. Geophys. Geosyst.* **14**, 4892–4905 (2013).
- E. T. Baker, *Geochem. Geophys. Geosyst.* **10**, Q06009 (2009).
- J. Dymond, *Geol. Soc. Am.* **154**, 133–174 (1981).
- G. B. Shimmield, N. B. Price, *Geochim. Cosmochim. Acta* **52**, 669–677 (1988).
- K. G. Speer, M. E. Maltud, A. M. Thurnherr, in *Energy and Mass Transfer in Hydrothermal Systems*, P. E. Halbach, V. Tunnicliffe, J. R. Hein, Eds. (Dahlem University Press, 2003), pp. 287–302.
- K. Bostrom, M. N. Peterson, O. Joensuu, D. E. Fisher, *J. Geophys. Res.* **74**, 3261–3270 (1969).
- M. Frank et al., *Paleoceanography* **9**, 559–578 (1994).
- Material and methods are available as supplemental materials on Science Online.
- C. R. German, S. Colley, M. R. Palmer, A. Khripounoff, G. P. Klinkhammer, *Deep Sea Res. Part I Oceanogr. Res. Pap.* **49**, 1921–1940 (2002).
- R. R. Cave, C. R. German, J. Thomson, R. W. Nesbitt, *Geochim. Cosmochim. Acta* **66**, 1905–1923 (2002).
- T. Schaller, J. Morford, S. R. Emerson, R. A. Feely, *Geochim. Cosmochim. Acta* **64**, 2243–2254 (2000).
- S. Emerson, J. I. Hedges, in *Treatise on Geochemistry*, K. K. Turekian, H. D. Holland, Eds. (Elsevier, vol. 6, 2004), pp. 293–319.
- J. A. Goff, *Science* **349**, 1065 (2015).
- J. A. Olive et al., *Science* **350**, 310–313 (2015).
- P. U. Clark et al., *Science* **325**, 710–714 (2009).
- K. Key, S. Constable, L. Liu, A. Pommier, *Nature* **495**, 499–502 (2013).
- P. B. Kelemen, G. Hirth, N. Shimizu, M. Spiegelman, H. J. B. Dick, *Philos. Trans. R. Soc. Lond. A* **355**, 283–318 (1997).
- J. MacLennan, M. Jull, D. McKenzie, L. Slater, K. Gronvold, *Geochem. Geophys. Geosyst.* **3**, 1–25 (2002).
- P. Cartigny, F. Pineau, C. Aubaud, M. Javoy, *Earth Planet. Sci. Lett.* **265**, 672–685 (2008).
- J. M. A. Burley, R. F. Katz, *Earth Planet. Sci. Lett.* **426**, 246–258 (2015).
- M. Hofmann, M. A. Morales Maqueda, *Geophys. Res. Lett.* **36**, L03603 (2009).
- J. Emile-Geay, G. Madec, *Ocean Sci.* **5**, 203–217 (2009).
- P. Martin, D. Archer, D. W. Lea, *Paleoceanography* **20**, PA2015 (2005).
- D. K. Smith, H. Schouten, L. Montési, W. Zhu, *Earth Planet. Sci. Lett.* **371–372**, 6–15 (2013).
- L. E. Lisiecki, M. E. Raymo, *Paleoceanography* **20**, PA1003 (2005).

ACKNOWLEDGMENTS

We dedicate this paper to J. Dymond, whose 1981 treatise on Nazca plate sediments made this work possible. We are also indebted to the Oregon State University Core Repository for carefully preserving the EPR sediment cores since they were collected in the early 1970s. We are grateful to L. Wingate at the University of Michigan and M. Cote at the University of Connecticut for technical support. This work has benefited from discussions with J. Granger, P. Vlahos, B. Fitzgerald, and M. Lyle. Data presented here are available on the National Oceanic and Atmospheric Administration's Paleoclimatology Data website

(www.ncdc.noaa.gov/data-access/paleoclimatology-data). Funding was provided by the University of Michigan and the University of Connecticut.

SUPPLEMENTARY MATERIALS

www.sciencemag.org/content/351/6272/478/suppl/DC1
Materials and Methods
Supplementary Text
Figs. S1 to S11
Tables S1 to S5
References (31–45)

14 September 2015; accepted 6 January 2016
10.1126/science.aad4296

HISTORY OF SCIENCE

Ancient Babylonian astronomers calculated Jupiter's position from the area under a time-velocity graph

Mathieu Ossendrijver*

The idea of computing a body's displacement as an area in time-velocity space is usually traced back to 14th-century Europe. I show that in four ancient Babylonian cuneiform tablets, Jupiter's displacement along the ecliptic is computed as the area of a trapezoidal figure obtained by drawing its daily displacement against time. This interpretation is prompted by a newly discovered tablet on which the same computation is presented in an equivalent arithmetical formulation. The tablets date from 350 to 50 BCE. The trapezoid procedures offer the first evidence for the use of geometrical methods in Babylonian mathematical astronomy, which was thus far viewed as operating exclusively with arithmetical concepts.

The so-called trapezoid procedures examined in this paper have long puzzled historians of Babylonian astronomy. They belong to the corpus of Babylonian mathematical astronomy, which comprises about 450 tablets from Babylon and Uruk dating between 400 and 50 BCE. Approximately 340 of these tablets are tables with computed planetary or lunar data arranged in rows and columns (1). The remaining 110 tablets are procedure texts with computational instructions (2), mostly aimed at computing or verifying the tables. In all of these texts the zodiac, invented in Babylonia near the end of the fifth century BCE (3), is used as a coordinate system for computing celestial positions. The underlying algorithms are structured as branching chains of arithmetical operations (additions, subtractions, and multiplications) that can be represented as flow charts (2). Geometrical concepts are conspicuously absent from these texts, whereas they are very common in the Babylonian mathematical corpus (4–7). Currently four tablets, most likely written in Babylon between 350 and 50 BCE, are known to preserve portions of a trapezoid procedure (8). Of the four procedures, here labeled B to E (figs. S1 to S4), one (B) preserves a mention of Jupiter and three (B, C, E) are embedded

in compendia of procedures dealing exclusively with Jupiter. The previously unpublished text D probably belongs to a similar compendium for Jupiter. In spite of these indications of a connection with Jupiter, their astronomical significance was previously not acknowledged or understood (1, 2, 6).

A recently discovered tablet containing an unpublished procedure text, here labeled text A (Fig. 1), sheds new light on the trapezoid procedures. Text A most likely originates from the same period and location (Babylon) as texts B to E (8). It contains a nearly complete set of instructions for Jupiter's motion along the ecliptic in accordance with the so-called scheme X.S₁ (2). Before the discovery of text A, this scheme was too fragmentarily known for identifying its connection with the trapezoid procedures. Covering one complete synodic cycle, scheme X.S₁ begins with Jupiter's heliacal rising (first visible rising at dawn), continuing with its first station (beginning of apparent retrograde motion), acronychal rising (last visible rising at dusk), second station (end of retrograde motion), and heliacal setting (last visible setting at dusk) (2). Scheme X.S₁ and the four trapezoid procedures are here shown to contain or imply mathematically equivalent descriptions of Jupiter's motion during the first 60 days after its first appearance. Whereas scheme X.S₁ employs a purely arithmetical terminology, the trapezoid procedures operate with geometrical entities.

Excellence Cluster TOPOI—Institute of Philosophy, Humboldt University, Berlin, Germany.

*Corresponding author. E-mail: mathieu.ossendrijver@hu-berlin.de